ACS APPLIED MATERIALS & INTERFACES

www.acsami.org

Forum Article

Nucleation of Pitting and Evolution of Stripping on Lithium-Metal Anodes

Hanrui Zhang,† Mert Ulusel,† and Feifei Shi*

Cite This: https://doi.org/10.1021/acsami.4c01530

Read Online

ACCESS | Metrics & More | Article Recommendations | Supporting Information

ABSTRACT: The stripping reaction of lithium (Li) will greatly impact the cyclability and safety of Li-metal batteries. However, Li pits' nucleation and growth, the origin of uneven stripping, are still poorly understood. In this study, we analyze the nucleation mechanism of Li pits and their morphology evolution with a large population and electrode area (>0.45 cm^2). We elucidate the dependence of the pit size and density on the current density and overpotential, which are aligned with classical nucleation theory. With a confocal laser scanning microscope, we reveal the preferential stripping on certain crystal grains and a new stripping mode between pure pitting and stripping without pitting. Descriptors like circularity and the aspect ratio (R) of the pit radius to depth are used to quantify the evolution of Li pits in three dimensions. As the pits grow, growth predominates along the through-planedirection, surpassing the expanding rate in the in-plane direction. After analyzing more than 1000 pits at each condition, we validate that the overpotential is inversely related to the pit radius and exponentially related to the rate of nucleation. With this established nucleation−overpotential relationship, we can better understand and predict the evolution of the surface area and roughness of Li electrodes under different stripping conditions. The knowledge and methodology developed in this work will significantly benefit Li-metal batteries' charging/discharging profile design and the assessment of large-scale Li-metal foils.

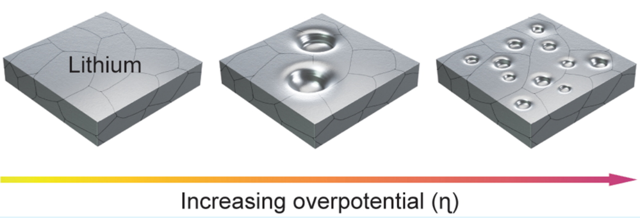

KEYWORDS: *nucleation of pitting, classical nucleation theory, lithium stripping, lithium-metal battery, confocal laser scanning microscopy (CLSM), evolution of pits*

INTRODUCTION

With electric vehicles (EVs) starting to see mainstream use, the demand for high-energy-density batteries is higher than ever.[1,2] Compared to the current graphite anode, the lithium (Li)-metal battery is a promising candidate for next-generation EV batteries due to its high theoretical capacity (3860 mAh g^{-1}) and low chemical potential.[3] Despite these advantages, Li-metal anodes suffer from poor reversibility during the deposition/stripping processes.[4] Such uncontrollable deposition and stripping processes on Li-metal anodes prevent their industrial deployment.[5] Li stripping is an electrochemical process of the anodic dissolution of Li$^+$. High-rate Li dissolution usually causes pitting, which exposes fresh metallic Li to the organic electrolyte, forming a solid−electrolyte interphase (SEI) and influencing Li deposition in subsequent cycles.[6] Unlike the extensively studied Li deposition process, the number of studies for Li stripping is relatively small.[7,8] These studies focused on the morphology of Li after cycles and electrode polarization in the two-electrode system[9,10] and paid less attention to the early-stage stripping at the initial cycle. Nonuniform stripping will alter the surface roughness and lead to dendritic Li deposition, negatively impacting subsequent deposition/stripping cycles.[8,9,11−13] Hence, it is critical to understand the mechanism of Li stripping and develop new strategies to facilitate uniform stripping.

In most of the morphology studies of Li deposition/stripping, optical microscopy (OM),[6,14,15] scanning electron microscopy (SEM),[7,16,17] and transmission electron microscopy[13,18,19] are widely used. Pei et al. used OM to study the nucleation and growth of electrodeposited Li on the copper (Cu) current collector.[20] Wood et al. utilized OM to observe Li morphology evolution during the cycling process, demonstrating that dendrites preferentially formed within the stripping pits.[14] However, these tools are limited to only in-plane or two-dimensional projection views on Li electrodes. Researchers recently started using tools such as focused-ion-beam (FIB)-SEM and three-dimensional (3D) microscopy to obtain a cross-sectional area and 3D reconstruction. Shi et al. visualized nanovoid formation between the SEI and stripped Li with FIB-SEM.[7] However, 3D reconstruction methods with

Special Issue: Early Career Forum 2024

Received: January 26, 2024
Revised: March 21, 2024
Accepted: April 11, 2024

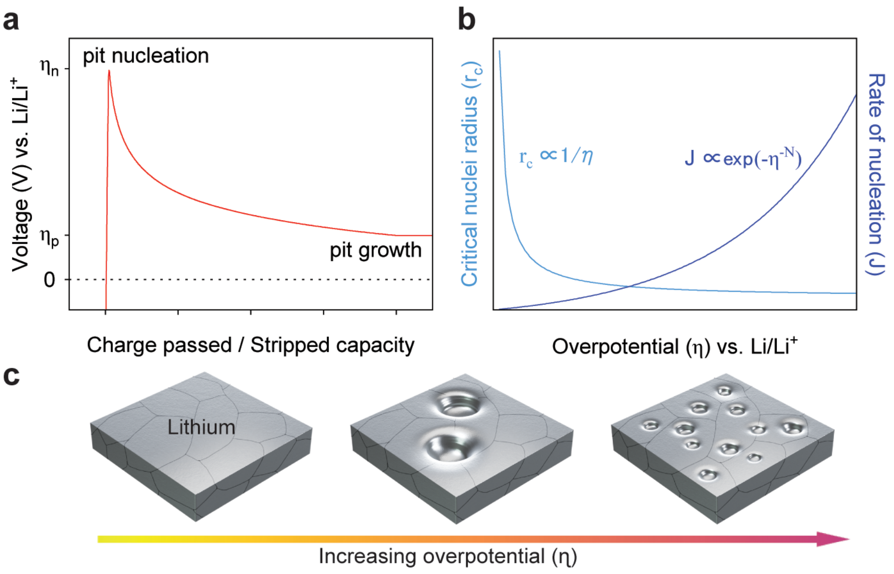

Figure 1. Fundamentals of Li pit nucleation. (a) Schematic of typical voltage profiles of galvanostatic Li stripping. The overpotential is divided into a nucleation overpotential (η_n) and plateau growth overpotential (η_p). (b) Schematic plot of the dependence of the critical nuclei radius r_c (light blue) and rate of nucleation J (dark blue) on the Li stripping overpotential, where the N denotes a constant. (c) Schematic illustration showing that stripping is driven by overpotentials.

ion milling/sputtering are intrinsically destructive and time-consuming to remove layers of sample.[21] Sanchez et al. used operando OM to study the morphology evolution of the pit and found anisotropic pit expansion in both the in-plane and through-plane directions.[6,15] White-light interferometry and confocal laser scanning microscopy (CLSM) are typical noncontact optical methods for 3D reconstruction of the surface morphology.[22] These white-light and laser-facilitated 3D microscopies have great potential to perform high-throughput screening of Li electrodes with a noncontact mode.

Besides characterization tools, the nucleation behavior of metal pitting is challenging to study due to its stochastic behavior.[23] Even under the same experimental conditions, the pits' size, shape, and distribution on the same batch of electrodes may vary. Statistical analysis of larger groups of samples and pits is crucial for extracting meaningful insights from the experimental data and assessing the reliability of the results. Although valuable knowledge has been provided in previous Li pitting studies, only a limited area of interest (typically micro/nanoscale) and a small number of pits (<20–50) were examined.[9,15,16,24] It is well-known that Li stripping depends on multiple factors, like the crystallographic orientation,[24,25] electrolyte,[24] SEI,[26,27] surface finishing,[28] and electrochemical conditions.[16,29] Nonuniformities on the surface, like grain boundaries and slip lines, will further accelerate the local dissolution of Li.[7] Besides the sampling size and homogeneity of Li electrodes, it is essential to mitigate human interference during sample preparation and data selection.[30] Automating the image processing to denoise and enhance images allows for more complex operations to be applicable with minimal artificial effects.[31] Hence, it is essential to develop automatic processing on a well-controlled Li-metal anode with a large enough data density to understand Li pitting comprehensively.

This study focuses on understanding the stripping behavior of a smoothed Li-metal anode. A homemade Li-metal anode (150 μm) is prepared and aged 24 h in 1 M LiPF$_6$ in ethylene carbonate and diethyl carbonate [1:1 (v/v)], i.e., LP40 electrolyte, due to its wide application in Li-ion batteries.[32] First, we examine the Li pit size distribution under various currents (>1000 pits/condition). Second, we explore the pit evolution in both the in-plane and through-plane directions with CLSM, quantifying the contribution between pitting and stripping without pitting under different currents. We classify the stripping process into three modes: stripping with pitting, stripping without pitting, and a mixed type by precise overpotential measurements using a three-electrode method. The circularity and aspect ratio (R) of the pit radius/depth are used as descriptors to assess the morphology evolution of pits (>400 counts) in both the in-plane and through-plane directions. Last, we correlate the pit size and rate of nucleation with the overpotential and monitor the surface area and roughness evolution under various stripping conditions. Statistical analysis of Li pitting (e.g., pit size, shape, density, and growth rate) provides a comprehensive understanding of the nucleation mechanism.

■ DISCUSSION

Fundamentals of Nucleation. While the deposition and stripping processes of Li are reversible thermodynamic processes, they are quite distinct. The electrodeposition process is usually limited by the diffusion of Li$^+$ in the electrolyte, while the vacancy diffusion in metallic Li and Li$^+$ conducting through the SEI governs the stripping process.[7,20] Figure 1a shows the typical galvanostatic curve of Li stripping on Li metal with a SEI. Usually, there are two overpotentials during stripping: (1) the nucleation overpotential (η_n), representing the voltage spike magnitude at the onset of pitting, and (2) the plateau overpotential (η_p), indicating the equilibrium voltage of Li stripping after pitting. In the early stage stripping, the Li electrode's potential increases to above 0 V vs Li/Li$^+$ to η_n, which drives the nucleation of small voids (i.e., pit nuclei). After the formation of pit nuclei, the overpotential gradually drops to η_p, which is smaller than that of η_n. Removing a Li atom from an existing void is more favorable, and expanding existing pit nuclei has a lower energy

https://doi.org/10.1021/acsami.4c01530

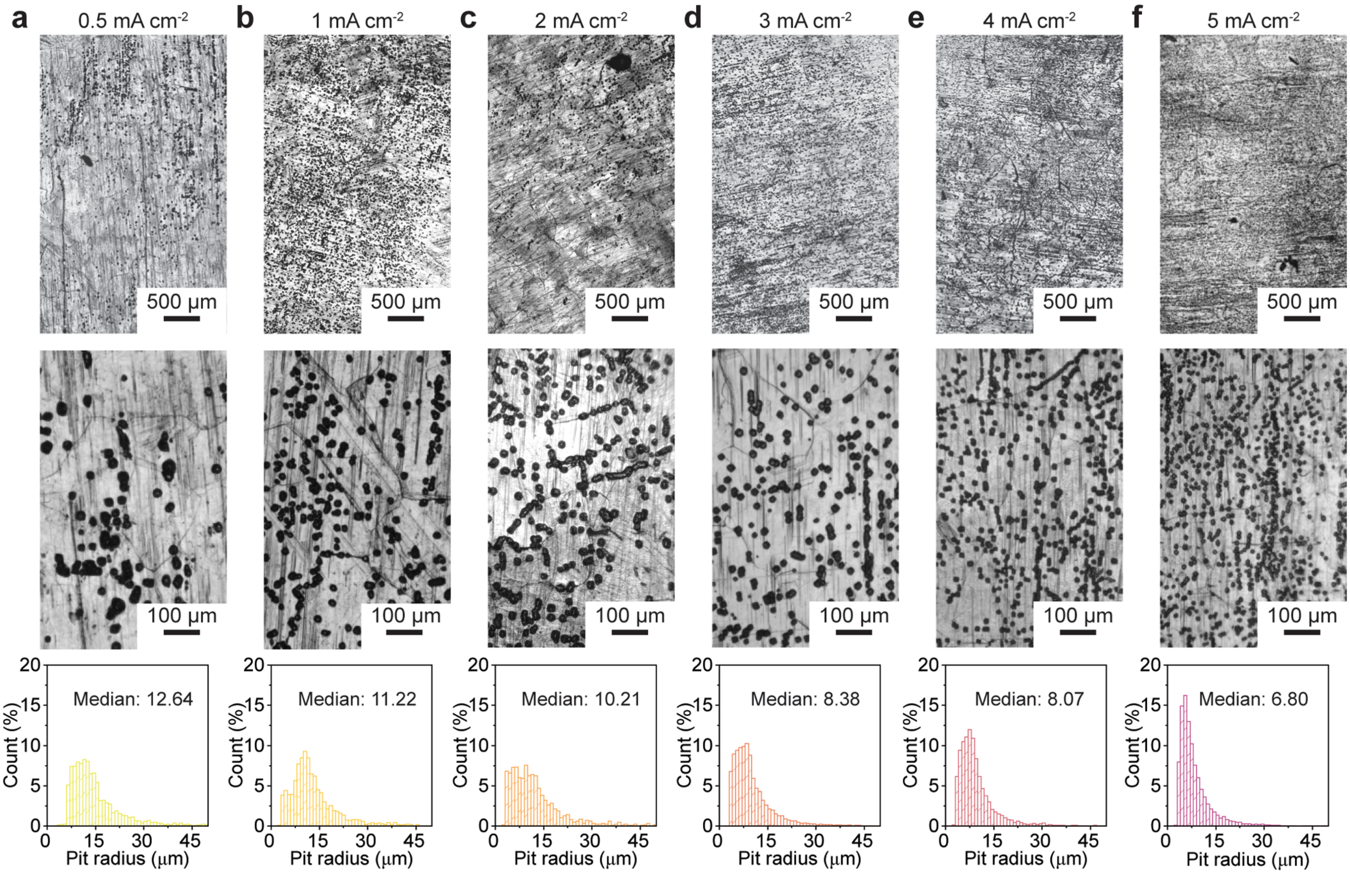

Figure 2. Pit size on a Li-metal anode with various stripping current densities (mA cm^{-2}): (a) 0.5; (b) 1; (c) 2; (d) 3; (e) 4; (f) 5. The stripping capacity is fixed at 0.2 mAh cm^{-2}. The bottom row is the pit radius distribution, where the bin size is 1 μm. Each condition is repeated over six times, and 1000−10000 pits are counted. The images are collected from the samples with overpotentials falling in the middle range. The total area of the top row is 10 mm^2, and the total area of the middle row is 0.4 mm^2.

barrier.[33] In this stage, the nuclei keep growing to form large size pits. According to classical nucleation theory (CNT), the total Gibbs free energy change for the nucleation is the sum of the surface energy change and volume energy change,[34] in eq 1:

$$\Delta G_{\mathrm{nucl}} = \Delta G_{\mathrm{bulk}} + \Delta G_{\mathrm{surf}} = A\gamma + V\Delta G_{\mathrm{V}} \tag{1}$$

where A is the surface area change, γ is the interfacial energy, V is the volume change, and ΔG_V is the free-energy difference per volume.

CNT has been successfully applied to the electrodeposition of metal and gas evolution in electrochemical reactions.[35−37] However, its applicability to Li pitting nucleation remains unexplored. The electrochemical curves of nucleation during the Li deposition and stripping process look very similar. The morphology of the Li nuclei tends to form spherical shapes in deposition processes to minimize the surface energy change.[34] If the stripping process follows a similar process, pits will form nuclei with a hemisphere shape (volume decreasing $2\pi r^3/3$). The total surface area change is the difference between a hemisphere and a flat circle (πr^2). It has been demonstrated that the critical nuclei size is proportional to the inverse of the overpotential ($1/\eta$) for the nucleation of Li on a Cu substrate.[20] In CNT, the critical radius (r_c) refers to the radius after which the addition of new atoms to the nuclei will reduce the overall free energy. Thus, nuclei with larger radii grow and nuclei with smaller radii shrink. . This concept is particularly relevant in the study of phase transitions, such as forming crystals from a liquid or gas or the reverse procedure. r_c is given in eq 2:

$$r_{\mathrm{c}} = \frac{\gamma}{\Delta G_{\mathrm{V}}} = \frac{\gamma}{ne\eta}V_{\mathrm{a}} \tag{2}$$

In this equation, n is the number of electrons, e is the elementary charge of the electron, η is the overpotential for nucleation, and V_a is the atomic volume of Li. This equation indicates that the increasing overpotential facilitates the nucleation of pitting by decreasing the critical radius.

Figure 1b illustrates the relationship among the critical nuclei radius (r_c), rate of nucleation ($J = dN/dt$, where N is the nuclei density), and overpotential (η). The critical nuclei radius demonstrates an inverse proportionality to the overpotential, indicating that larger overpotentials result in smaller nuclei. From the Arrhenius rate expression for nucleation, the overpotential has an exponential relationship with the rate of nucleation.[38,39] At low overpotentials, the critical radius approaches infinity, and the nuclei density is close to zero, suggesting an absence of pitting, as shown in Figure S1 (0.1 mA cm^{-2}). As the overpotential increases, the critical radius decreases significantly, tending toward zero at high overpotentials, corresponding to a substantial increase in the nuclei density. It is important to clarify that r_c represents the size of the initial nuclei, not the size of the pits observed at the microscale. However, the final size of these pits is proportional

https://doi.org/10.1021/acsami.4c01530

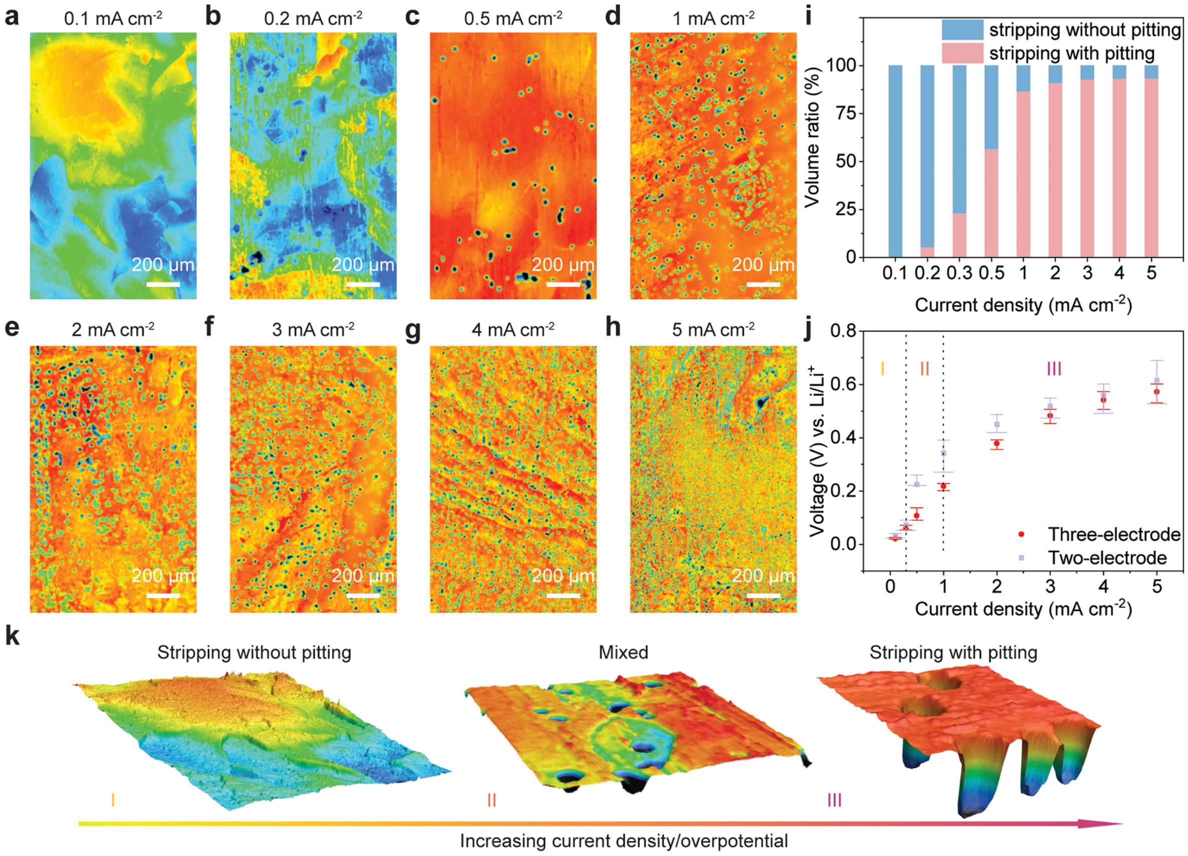

Figure 3. Critical current and overpotential for pitting nucleation. The morphology of stripped Li. The stripped capacity is 0.2 mAh cm^{-2} under current values of (a) 0.1, (b) 0.2, (c) 0.5, (d) 1, (e) 2, (f) 3, (g) 4, and (h) 5 mA cm^{-2}. The dimension of each image is 1 × 1.6 mm. (i) Volume ratio of pits during the stripping under various current densities. The total stripped volume of Li is calculated based on the theoretical capacity. (j) Stripping nucleation overpotential measured by a two-electrode coin cell and a three-electrode Swagelok cell. Region I: stripping without a pitting region. Region II: mixed region. Region III: pitting region. (k) Scheme of the transition of stripping with increasing overpotential. Scale bar: 200 μm.

to the initial size of the nuclei under the fixed stripping capacity. The rate of nucleation has an exponential relationship with the overpotential. Figure 1c shows a schematic of the pitting evolution on the Li surface as the overpotential (η) increases. Based on CNT, higher overpotentials promote nucleation, increasing the number of nuclei and decreasing the critical radius of the nuclei.

Here, we prepare the lab-made Li-metal anode (150 μm) out of commercial Li foils to lower the surface roughness, as shown in Figures S1−S3. To validate the overpotential effect for the Li pit radius, we use various current densities of 0.5−5 mA cm^{-2} to tune the overpotential under different charging rates with a fixed capacity of 0.2 mAh cm^{-2} in a LP40 electrolyte. The lowest current density is chosen as 0.5 mA cm^{-2} to observe a sufficient quantity of pits. As at low current densities, pits are fewer and more randomly dispersed. The area capacity is determined to avoid the merging of individual pits. Each current density is repeated more than six times, as depicted in the scattered plots in Figure S1a. Figure S1b shows the characteristic voltage profiles for Li stripping. The ex-situ OM images are used to image the stripped Li, which is located within an argon-filled glovebox (O_2 and H_2O level <0.1 ppm), as exhibited in Figure S4, so there is no exposure to ambient air during the sample preparation and transfer. The morphology of stripped Li metal collected by OM is shown in Figure 2. At a low current density of 0.5 mA cm^{-2} (Figure 2a), pits are distributed heterogeneously across the surface, where nucleation has occurred preferentially at certain sites on the surface, while other regions are vacant. Because a low current density corresponds to a low nucleation overpotential, the driving force for the nucleation reaction is comparatively low, with the pits preferentially nucleating at low-energy barrier sites.[15] The distribution of the pit sizes is asymmetric because pits nucleated near each other tend to merge during the growth phase.[6] With increasing current density at a fixed stripping capacity from 1 to 2 mA cm^{-2}, the nucleation density increases while the pit radius decreases, as seen in Figure 2c,d. When the current density increases to 4−5 mA cm^{-2} (Figure 2e,f), the radius keeps decreasing with increasing nuclei density, and pits start to overlap. Above 5 mA cm^{-2}, the overlapping will be more severe and it will be challenging to segregate individual pits for the subsequent imaging processing.

For pit size and density measurements, 3 × 3 grids of 5× magnification images are taken, covering an area of 0.45 cm^2 (about half of the Li electrode area). Preprocessing and analysis of the OM images are automated using MATLAB. The images are collected from the samples with overpotentials falling in the middle range. Images are further denoised using elementary image processing methods, and the dark regions corresponding to pits are segmented and analyzed. The circle-equivalent diameter is used to quantify the pit sizes because highly asymmetric pits are also present on sample surfaces.

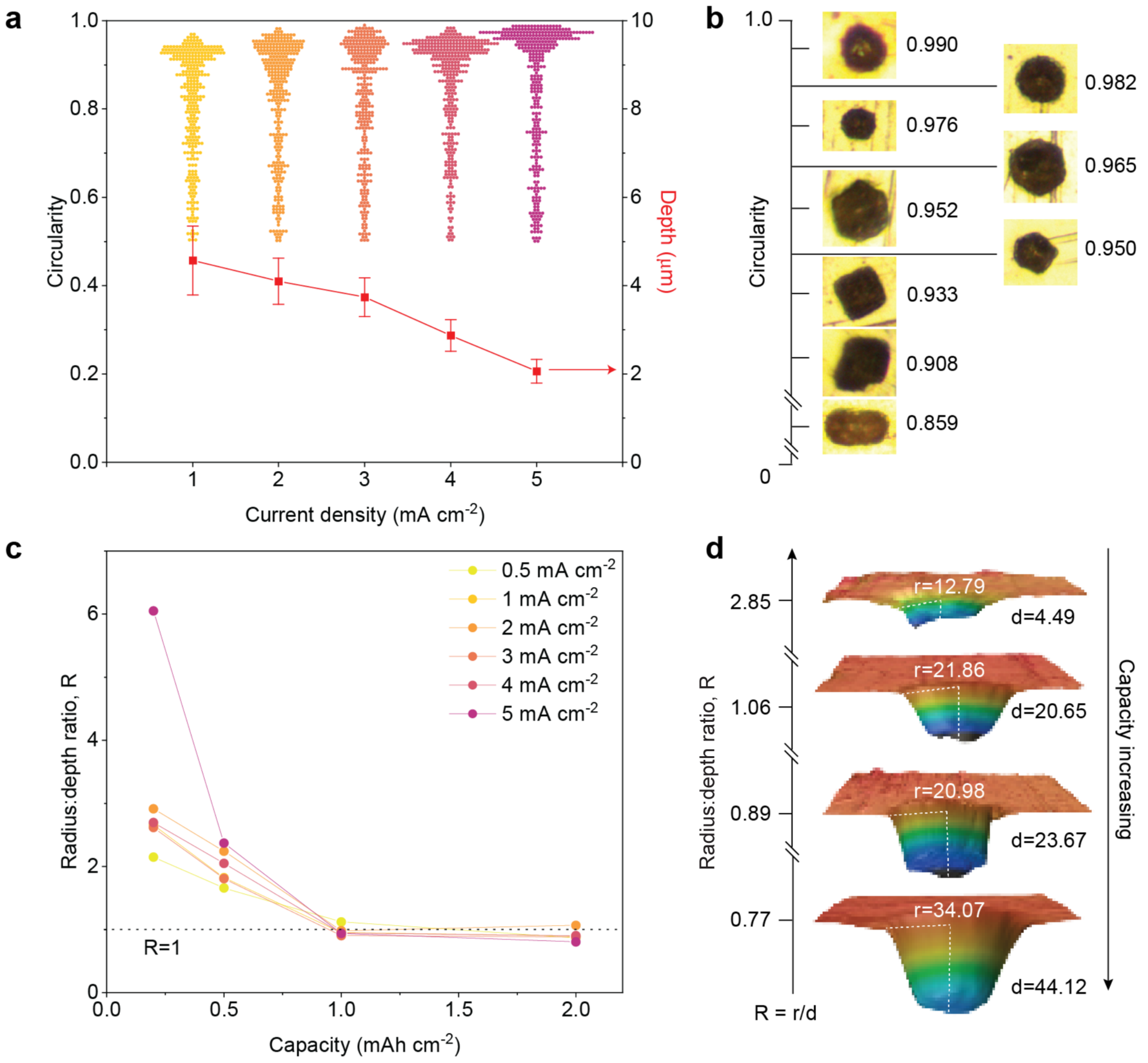

Figure 4. Evolution of pits via the in-plane and through-plane directions. (a) Circularity and depth of pits that are stripped under various current densities. The stripped capacity is fixed at 0.2 mAh cm^{-2}, and over 300 pits are counted. (b) OM images of selected pits and their circularity. (c) Evolution of the ratio between the pit radius and depth of the stripped pits under various current densities and capacities. Over 300 pits are counted. (d) Cross sections of typical pits. The aspect ratio R = pit radius/depth shows the expansion rate along the in-plane and through-plane directions.

(Details are given in Figures S5 and S6 and Supplementary Notes S3 and S4). This allows for an enormous volume of data to be produced for a larger sample (e.g., centimeter-scale). We first explore the pit number effect in Figure S7 (50 vs 1000 vs 5000 pits), finding that the histograms become smoother and more continuous as the number of pits increases from 50 to 1000. The histogram distribution is very similar for 1000 vs 5000 pits. The pit size distribution histogram is exhibited in the bottom row of Figure 2. A size filter is applied for pits with radii of <5 μm because it is hard to differentiate small pits from dirt or scratches. Another filter is applied for pits with radii of >50 μm, which comes from the overlapping of multiple pits. When the current density is 0.5 mA cm^{-2}, the median pit radius is 12.64 μm. As the current density rises to 1 and 2 mA cm^{-2}, the median pit radii decrease to 11.22 and 10.221 μm, respectively. The increased overpotential at higher current densities results in more nuclei, yet it also limits pit growth, reducing the median pit size. As the current density reaches 3, 4, and 5 mA cm^{-2}, the median pit radius gradually decreases to 8.38, 8.07, and 6.80 μm, respectively. The increased overpotential at higher current densities results in more nuclei, reducing the median pit radius. The correlation between the nucleation radius and overpotential aligns well with CNT, where an increasing driving force results in a lower critical radius for nucleation.

Critical Current and Overpotential for Pitting. Besides the size distribution from the in-plane view, we further study the 3D morphology of Li pits using a CLSM instrument (VK-X3100, Keyence). Compared to the OM white-light interferometer, CLSM offers enhanced differentiation between the substrate and stripping pits, providing high-accuracy depth information on pits with steep angles.[40] In Figure 3a,b, under the low current density of 0.1 mA cm^{-2}, some grains are lower than the average height with no presence of pits, indicating the preferential stripping behavior on certain crystal orientations. Such behavior is analogous to the anisotropic corrosion of other metals, where different crystal planes exhibit varying degrees of reactivity to corrosion.[41,42] A computational study

https://doi.org/10.1021/acsami.4c01530
ACS Appl. Mater. Interfaces XXXX, XXX, XXX−XXX

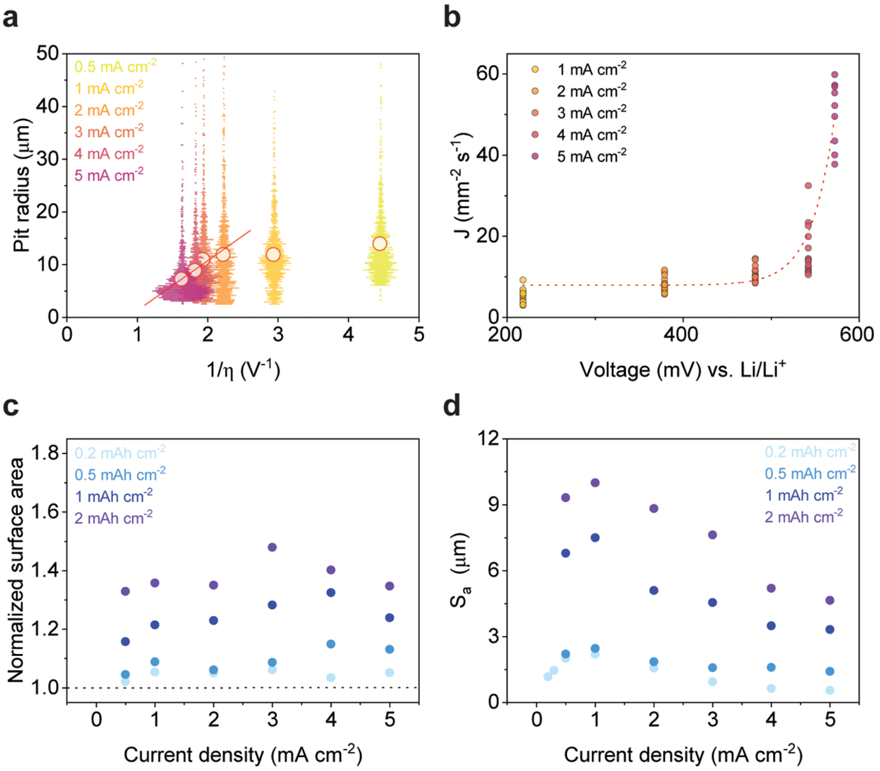

Figure 5. Li pitting nucleation mechanism. (a) Correlation between the pit radius and the inverse of the overpotential under different stripping current densities. The hollow circle denotes the median value of the pit radius. More than 1000 pits are counted, which are generated under the fixed stripping capacity of 0.2 mAh cm^{-2}. (b) Correlation between the rate of nucleation J and overpotential. Under each condition, J is analyzed from over nine coin cells. The overpotentials are normalized from the three-electrode cell results. (c) Normalized surface area of a Li-metal electrode under current densities (0.5, 1, 2, 3, 4, and 5 mA cm^{-2}) and stripped capacities (0.2, 0.5, 1, and 2 mAh cm^{-2}). The normalized surface area is calculated from the actual surface area divided by the geometric surface area. (d) Evolution of the arithmetical mean height (S_a) under different current densities and capacities. S_a is calculated by averaging the absolute values of the surface height deviations from the average plane.

predicts that (100) Li planes possess the lowest vacancy solubility and highest intervacancy interactions, leading to nondirectional pitting upon exposure to the electrolyte.[25] Since mechanical rolling will generate (100) out-of-plane texture, grains with (100) orientations will be preferentially stripped, leaving a height contrast across the surface. This height contrast (<10 μm) is overlooked in the previous studies because it is hard to capture by OM or SEM. As shown in Figure 3c,d, when the current density increases to 0.2−0.5 mA cm^{-2}, pits start to be observed and tend to form at areas such as the grain boundary and slip lines due to elevated ionic conductivity.[7] The preferential stripping of certain grains still exists with pitting behavior. In Figure 3e−h, stripping is dominated by randomly dispersed pits when the current density is ≥1 mA cm^{-2}. As discussed in the previous section, there is a rise in the nuclei density corresponding to an increase in the current density and overpotential, accompanied by a decrease in the pit radius and depth.

To quantify the contribution between pitting and stripping without pitting, we first measure the cumulative volume of pits during different current density stripping, as shown in Figure 3i. Given that the total volume stripped (capacity) remains constant, we further extract the stripped volume ratio between the pitting and stripping without pitting. The volume of pitting is measured and calculated by CLSM, and the rest of the volume comes from the stripping without pitting, based on the theoretical volume value. Under a critical current density of 0.2 mA cm^{-2}, pitting contributes a tiny portion to the total stripping volume (<5.6 vol %), indicating that stripping without pitting is the dominant mode. At 0.5 mA cm^{-2}, about 56.7% of the volume is stripped by pitting, indicating that stripping with/without pitting coexists. Beyond 1 mA cm^{-2}, pitting dominates stripping (>86.8 vol %). The three-electrode setup can accurately measure the nucleation of stripping by adding the half-cycled $Li_4Ti_5O_{12}$ (LTO) reference electrode.[43] Figure 3j compares the two-electrode and three-electrode setups. Both methods show a higher overpotential under a larger current density. Under a critical current density of 0.2 mA, the onset overpotential for pitting nucleation is determined at ∼100 mV vs Li/Li$^+$. This overpotential is consistent with the onset potential of pitting in carbonate and ether electrolytes reported in the previous literature.[7] This overpotential drifts to 0.2 V in a two-electrode setup due to polarization. Interestingly, the overpotential trend in Figure 3j mirrors the pitting trend in Figure 3i, validating that the overpotential drives the Li-pitting process.

Based on the morphological observation of pitting and stripping without pitting and careful study of the overpotential−current relationship, we categorize the three stripping modes in Figure 3k. For mode I (<0.2 mA cm^{-2} or overpotential <100 mV), under low current density/overpotential, there is no pitting due to the low driving force. In this mode, stripping prefers certain grains without pitting, analogous to anisotropic corrosion. In mode II (0.2−1 mA cm^{-2} or overpotential between 100 and 200 mV), the overpotential is high enough (surpassed 0.1 V) to trigger SEI layer breakdown and pitting initiation, and a mixed stripping mode coexists. The stochastic behavior of pitting is more pronounced at its initial stage, as shown in the error bar in Figure 3j. For mode III (>1 mA cm^{-2} or overpotential of >200 mV), at elevated overpotential, the kinetics is the dominant factor, and pitting is the only mode for stripping. This is the first time that the transition between mode I and mode III has been captured and quantified.

Evolution of Pits via the In-Plane and Through-Plane Directions. Besides pit size analysis, the pits' shape and depth evolution are less known and cannot be predicted based on any existing nucleation theory. Previous studies observed the anisotropic expansion of individual pits, indicating that the pit expansion is anisotropic in both the in-plane and through-plane directions.[6] Circularity is used as a measure to quantify the shapes of different pits. It can serve as a crucial parameter describing the symmetry and regularity of the nucleation process. The circularity (C) is calculated based on the equation $C = \frac{4\pi A}{P^2}$, where A represents the area of the pit and P is its perimeter. In the case of a perfectly circular shape, C attains a value of 1. In Figure 4a, we summarize the circularity of pits under current densities at 1−5 mA cm^{-2} with a fixed capacity of 0.2 mAh cm^{-2}. At low current densities like 1 mA cm^{-2}, the circularity of pits is broadly distributed compared to that under higher current densities (5 mA cm^{-2}). This phenomenon is analogous to pitting corrosion for other metals.[44,45] Under a low reaction rate (i.e., current density), the pits' growth is near-equilibrium, and crystallographic effects control the reaction rate,[46] forming pits with various geometric shapes depending on the degree of anisotropy between the different orientations.[47] In contrast, hemispherical pits with circular electropolished interiors or polished pits form at high reaction rates. Figure S9 and Supplementary Note S5 show the image processing procedure, with over 300 pits chosen for each current density. Examples of typical non-circular pits are shown in Figures 4b and S10.

Besides the current density, the capacity will influence the pit morphology during pit nuclei growth. Figures S11 and S12 depict the effect of the capacity on pitting-based stripping. As the capacity increases from 0.5 to 2 mAh cm^{-2}, the pits expand in both the in-plane and through-plane directions. To quantify the competition among different planes, we calculated the aspect ratio of the average pit radius to the maximum pit depth, as summarized in Figure 4c. For hemispherical pits, their aspect ratio is near 1, indicating the isotropic growth of the pit. Under a current density of 5 mA cm^{-2} with an areal capacity of 0.2 mAh cm^{-2}, the aspect ratio is as large as 6, indicating that the pits are shallow. As the capacity increases to 2 mAh cm^{-2}, the aspect ratio approaches 1. All other conditions (1−5 mA cm^{-2}) follow a similar trend. The pit gradually grows to a hemisphere-like shape. This phenomenon is consistent with surface energy minimization.[34] The schematic representation of the stripping evolution is summarized in Figure 4d. The newly formed pit possesses a wide and shallow shape, gradually evolving into a hemisphere with increasing stripping capacity as R keeps decreasing.

Nucleation Mechanism and Growth of Li Pits. Based on our observation of Figure 2, both higher current densities and overpotentials lead to a large pit size and density. Random regions in the central area of each electrode are chosen for analysis with over 1000 pits. To examine the applicability of CNT to the nucleation of Li pits, we plotted the pit radius inverse overpotential in Figure 5a. A good linear fitting appears under large overpotentials, i.e., current densities from 2 to 5 mA cm^{-2}. For smaller overpotentials at 0.5−1 mA cm^{-2}, the median pit radius does not lie on the linear fitting because not all of the capacity is stripped by pitting. According to CNT, larger overpotentials will easily overcome the nucleation barrier and cause a faster formation rate. Such fast reaction kinetics of pitting can easily override the other effects (e.g., grain orientations and boundaries). The rate of nucleation per unit area is calculated and is given in Figure 5b. The nucleation time is determined by the intersection of the tangent line of the nucleation and growth process, and the details are shown in Figure S14. The rate of nucleation shows an exponential relationship with the overpotential, ranging from 3 to 55 mm^{-2} s^{-1}, because there is a sharp transition between 500 and 550 mV vs Li/Li^{+}. The pit radius and rate of nucleation trend comply well with CNT. The rate of nucleation of Li stripping is much slower than that of Li deposition on Li[25] or Cu.[20]

During the Li-stripping process, the surface area of the electrode continuously changes, consuming more electrolyte to form the SEI and impacting the following cycle deposition of Li. This variation in the surface area will also affect the local current density and impedance during battery cycling. Hence, it is important to evaluate the true surface area of Li after stripping. As discussed in Figures 2 and 3 previously, small currents typically generate a lower density of large pits, while large current density leads to a high density of small pits. It is not apparent how these current and capacity conditions impact the surface area of the electrode. Here, we use the normalized surface area, which is calculated from the actual surface area divided by the geometric surface area, as a more reliable descriptor for the surface area change. In Figure 5c, we summarize and normalize the surface area of the Li-metal anode from the true surface area extracted by CLSM. Under all conditions, the normalized surface area evolves with increased stripping capacity. Besides, it can be seen that the normalized surface area reaches the maximum at 3 mA cm^{-2}. The total surface area is minimized because the low current densities introduce a low nuclei density. Under the high current conditions (≥5 mA cm^{-2}), the surface area is decreased due to the overlapping of pits.

Besides the surface area of the electrode, the arithmetical mean height (S_a) is another essential factor in forming a uniform electrical field and diffusion. Roughness typically refers to deviations in the direction of the normal vector of the surface from its ideal form, which is not necessarily aligned with the change in the surface area. Figure 5d depicts the S_a evolution of the Li surface under various stripping currents. S_a evolves with the increased stripping capacity for all current densities, indicating that the surface area changes significantly, reaching a maximum roughness under 1 mA cm^{-2}. Understanding the nucleation mechanism and growth of Li pits will guide the cycling profile for uniform Li stripping and follow cycle plating.[12]

CONCLUSION

This work systematically studies the early-stage nucleation and growth of Li pits under various current and overpotential conditions. Compared to the current, the overpotential shows a high correlation with both the pit size and the rate of nucleation, indicating that the overpotential is the driving force behind pit nucleation. Large overpotentials will lead to a small pit size and a high pit density. When the overpotential is below the critical value of ~100 mV, the Li atoms are uniformly stripped on preferential crystal grains without pitting. When the overpotential is between 100 and 200 mV, the pitting process initiates with uniform stripping. At large overpotential ($\geq$200 mV vs Li/Li$^+$) conditions, Li pitting is the dominant stripping mode. Besides the pit size and density, the overpotential also impacts the pit shape. Li pits appear in a circle shape in the in-plane view, under larger overpotentials. As the stripping capacity increases, through-plane direction growth predominates, surpassing the expansion rate in the in-plane direction. We quantify the 3D evolution of Li pits with the circularity and aspect ratio between the radius and depth (R). We also find that the pit radius is proportional to the inverse of the overpotential, and the overpotential has an exponential relationship with the rate of nucleation. Such knowledge of Li-pitting nucleation provides a great foundation to predict the morphological evolution of the Li-metal anode. We found that the size, density, and overlaid conditions of pits will determine the surface area and roughness of the stripped Li electrode, which will greatly benefit the design of the charging/discharging profile. The developed methodology can be further applied to the quality control of large-scale manufacturing of Li-metal foils.

EXPERIMENTAL SECTION

Thickness Reduction of Foils. The Li foils (Alf 750 μm) are thinned using a TMAXCN roller. Li is cut from the original Li foil and sealed in pouches inside the argon atmosphere in the glovebox. The pouches are then removed from the glovebox and rolled sequentially to the desired thicknesses. Li foils of 150 μm thickness are used to evaluate the effect of microstructural features.

Preparation of Cells. 2032-type coin cells are assembled using lithium (Li) and copper (Cu) electrodes as working and counter electrodes. Because Li quickly degrades upon contact with oxygen, all assembly and imaging are conducted inside the argon atmosphere Vigor glovebox. Lab-made 150 μm Li foils are used. Ethylene carbonate/diethyl carbonate [1:1 (v/v)] with 1 M lithium hexafluorophosphate ($LiPF_6$; LP40, Sigma-Aldrich) is used as the electrolyte for all experiments. The cells are pressed using a MSK-110 hydraulic crimping machine under a pressure of 1000 psi. The assembled cells are aged for 24 h to ensure uniform and consistent SEI layer formation. For the disassembly of cells, the MSK-110 hydraulic crimping machine is used with the disassembly apparatus to open the cells and remove the stripped Li foils. The foils are then immediately rinsed with diethyl carbonate to prevent the precipitation of Li salt on the surface, which potentially obscures other features during imaging.

Electrochemical Measurement. A LANDT battery test system 3200A is used to strip the Li anodes in the assembled cells. To test the effect of overpotentials, the cells are cycled with 0.1, 0.2, 0.3, 0.5, 1, 2, 3, 4, and 5 mA cm^{-2} current density under a constant capacity of 0.2 mAh m^{-2}. This capacity is chosen from preliminary data because a higher capacity results in the merging of pits and a low capacity makes it difficult to distinguish the pits with OM. Our experiments evaluate the stripping overpotential using both two-electrode (coin cell) and three-electrode (Swagelok cell) configurations to accurately measure the true stripping overpotential. In the two-electrode system, the measured overpotential is a combined value of both the stripping and deposition overpotentials, which cannot be distinguished separately. However, the three-electrode system can accurately determine the overpotential for stripping and deposition separately due to the additional reference electrode. For the three-electrode system, the working electrode is Li foil, the counter electrode is Cu foil, and the reference electrode is half-charged LTO.[7]

Imaging and Analysis. The anodes are imaged using a ME580TA-PZ-2L-18M3 optical microscope inside the glovebox. To count pits for size and density measurements, 3 × 3 grids of 5× magnification images are taken to cover a large electrode surface area. For shape evaluation, 10× magnification images are used for better resolution. MATLAB is used to isolate individual pits from OM images to measure their sizes and shapes. This allows for a large volume of data to be produced at a large sample size. The proposed pipeline for processing the acquired OM images follows: Apply a Gaussian filter and red-channel thresholding blend and dim unwanted features on the images such as scratches. Black and white thresholding is then used to highlight the wanted features. These regions can then be segmented, and their shapes and sizes can be individually evaluated. Because the pits are not perfectly circular and, in some cases, polygonal, their diameters can be measured with the equivalent circle diameter, while their shapes can be compared with the circularity ratio parameter. For the CLSM test, Li foil is sealed between a glass slide and a cover slide with Kapton tape, as shown in Figure S8. The samples can remain unaffected in ambient air for over 4 hours. The 3D morphology of Li pits is measured by VK-X3100 (Keyence). The images are taken with 20× and 50× lenses and stitched together as 3 cm × 3 cm. Analysis is done by the VK-X 3000 Multifile Analyzer software by Keyence.

ASSOCIATED CONTENT

Supporting Information

The Supporting Information is available free of charge at https://pubs.acs.org/doi/10.1021/acsami.4c01530.

> Derivation of nucleation equations, two-electrode overpotentials, surface roughness and XPS of lab-made Li foils, experiment setup of optical microscope, details of image processing, details of the pit diameter measurement, discussion the effect of the pit numbers, experiment setup of profilometer samples, details of circularity quantication method, capacity effect on stripping, and details of the rate of nucleation determination (PDF)

AUTHOR INFORMATION

Corresponding Author

Feifei Shi − *John and Willie Leone Family Department of Energy and Mineral Engineering, Pennsylvania State University, University Park, Pennsylvania 16802, United States; Department of Materials Science and Engineering, Pennsylvania State University, University Park, Pennsylvania 16802, United States;* orcid.org/0000-0002-2598-1867; Email: feifeishi@psu.edu

Authors

Hanrui Zhang − *John and Willie Leone Family Department of Energy and Mineral Engineering, Pennsylvania State University, University Park, Pennsylvania 16802, United States;* orcid.org/0000-0001-8576-9705

Mert Ulusel − *Department of Materials Science and Engineering, Pennsylvania State University, University Park, Pennsylvania 16802, United States*

Complete contact information is available at: https://pubs.acs.org/10.1021/acsami.4c01530

Author Contributions

[†]H.Z. and M.U. contributed equally to this work.

Notes

The authors declare no competing financial interest.

ACKNOWLEDGMENTS

H.Z., M.U., and F.S. are grateful for support from the Assistant Secretary for Energy Efficiency and Renewable Energy, Office of Vehicle Technologies of the U.S. Department of Energy through the Advanced Battery Materials Research Program. F.S. is grateful for support from the National Science Foundation under Grant 2239690. The coauthors acknowledge the use of the Penn State Materials Characterization Lab.

■ REFERENCES

(1) Yang, X.-G.; Liu, T.; Wang, C.-Y. Thermally modulated lithium iron phosphate batteries for mass-market electric vehicles. *Nature Energy* **2021**, *6* (2), 176−185.

(2) Xiao, J.; Shi, F.; Glossmann, T.; Burnett, C.; Liu, Z. From laboratory innovations to materials manufacturing for lithium-based batteries. *Nature Energy* **2023**, *8*, 329.

(3) Lin, D.; Liu, Y.; Cui, Y. Reviving the lithium metal anode for high-energy batteries. *Nat. Nanotechnol* **2017**, *12* (3), 194−206.

(4) Zhang, X.; Yang, Y.; Zhou, Z. Towards practical lithium-metal anodes. *Chem. Soc. Rev.* **2020**, *49* (10), 3040−3071.

(5) Jin, C.; Liu, T.; Sheng, O.; Li, M.; Liu, T.; Yuan, Y.; Nai, J.; Ju, Z.; Zhang, W.; Liu, Y.; et al. Rejuvenating dead lithium supply in lithium metal anodes by iodine redox. *Nature Energy* **2021**, *6* (4), 378−387.

(6) Sanchez, A. J.; Kazyak, E.; Chen, Y.; Lasso, J.; Dasgupta, N. P. Lithium stripping: anisotropic evolution and faceting of pits revealed byoperando3-D microscopy. *Journal of Materials Chemistry A* **2021**, *9* (37), 21013−21023.

(7) Shi, F.; Pei, A.; Boyle, D. T.; Xie, J.; Yu, X.; Zhang, X.; Cui, Y. Lithium metal stripping beneath the solid electrolyte interphase. *Proc. Natl. Acad. Sci. U. S. A.* **2018**, *115* (34), 8529−8534.

(8) Jiang, F.-N.; Yang, S.-J.; Liu, H.; Cheng, X.-B.; Liu, L.; Xiang, R.; Zhang, Q.; Kaskel, S.; Huang, J.-Q. Mechanism understanding for stripping electrochemistry of Li metal anode. *SusMat* **2021**, *1* (4), 506−536.

(9) Liu, H.; Cheng, X.-B.; Xu, R.; Zhang, X.-Q.; Yan, C.; Huang, J.-Q.; Zhang, Q. Plating/Stripping Behavior of Actual Lithium Metal Anode. *Adv. Energy Mater.* **2019**, *9* (44), No. 1902254.

(10) Kasemchainan, J.; Zekoll, S.; Spencer Jolly, D.; Ning, Z.; Hartley, G. O.; Marrow, J.; Bruce, P. G. Critical stripping current leads to dendrite formation on plating in lithium anode solid electrolyte cells. *Nat. Mater.* **2019**, *18* (10), 1105−1111.

(11) Yu, S.; Wang, S.; Miao, Q.; Hui, Z.; Hyun, G.; Holoubek, J.; Yu, X.; Gao, J.; Liu, P. Composite Lithium Metal Structure to Mitigate Pulverization and Enable Long-Life Batteries. *Adv. Energy Mater.* **2023**, *13* (40). DOI: 10.1002/aenm.202302400.

(12) Huang, Y. K.; Pan, R.; Rehnlund, D.; Wang, Z.; Nyholm, L. First-Cycle Oxidative Generation of Lithium Nucleation Sites Stabilizes Lithium-Metal Electrodes. *Adv. Energy Mater.* **2021**, *11* (9). DOI: 10.1002/aenm.202003674.

(13) Werres, M.; Xu, Y.; Jia, H.; Wang, C.; Xu, W.; Latz, A.; Horstmann, B. Origin of Heterogeneous Stripping of Lithium in Liquid Electrolytes. *ACS Nano* **2023**, *17* (11), 10218−10228.

(14) Wood, K. N.; Kazyak, E.; Chadwick, A. F.; Chen, K. H.; Zhang, J. G.; Thornton, K.; Dasgupta, N. P. Dendrites and Pits: Untangling the Complex Behavior of Lithium Metal Anodes through Operando Video Microscopy. *ACS Cent Sci.* **2016**, *2* (11), 790−801.

(15) Sanchez, A. J.; Kazyak, E.; Chen, Y.; Chen, K.-H.; Pattison, E. R.; Dasgupta, N. P. Plan-View Operando Video Microscopy of Li Metal Anodes: Identifying the Coupled Relationships among Nucleation, Morphology, and Reversibility. *ACS Energy Letters* **2020**, *5* (3), 994−1004.

(16) Sagane, F.; Shimokawa, R.; Sano, H.; Sakaebe, H.; Iriyama, Y. In-situ scanning electron microscopy observations of Li plating and stripping reactions at the lithium phosphorus oxynitride glass electrolyte/Cu interface. *J. Power Sources* **2013**, *225*, 245−250.

(17) von Lüders, C.; Keil, J.; Webersberger, M.; Jossen, A. Modeling of lithium plating and lithium stripping in lithium-ion batteries. *J. Power Sources* **2019**, *414*, 41−47.

(18) Lee, S.-Y.; Shangguan, J.; Betzler, S.; Harris, S. J.; Doeff, M. M.; Zheng, H. Lithium metal stripping mechanisms revealed through electrochemical liquid cell electron microscopy. *Nano Energy* **2022**, *102*, 107641.

(19) Wang, C.; Wang, H.; Tao, L.; Wang, X.; Cao, P.; Lin, F.; Xin, H. L. Direct Observation of Nucleation and Growth Behaviors of Lithium by In Situ Electron Microscopy. *ACS Energy Letters* **2023**, *8* (4), 1929−1935.

(20) Pei, A.; Zheng, G.; Shi, F.; Li, Y.; Cui, Y. Nanoscale Nucleation and Growth of Electrodeposited Lithium Metal. *Nano Lett.* **2017**, *17* (2), 1132−1139.

(21) Deng, Z.; Lin, X.; Huang, Z.; Meng, J.; Zhong, Y.; Ma, G.; Zhou, Y.; Shen, Y.; Ding, H.; Huang, Y. Recent Progress on Advanced Imaging Techniques for Lithium-Ion Batteries. *Adv. Energy Mater.* **2021**, *11* (2). DOI: 10.1002/aenm.202000806.

(22) Jiao, F.; Liu, L.; Cheng, W.; Li, C.; Zhang, X. Review of optical measurement techniques for measuring three-dimensional topography of inner-wall-shaped parts. *Measurement* **2022**, *202*, 111794.

(23) Velmurugan, J.; Noël, J.-M.; Nogala, W.; Mirkin, M. V. Nucleation and growth of metal on nanoelectrodes. *Chemical Science* **2012**, *3* (11), 3307.

(24) Huang, F.; Wang, S.; Jie, Y.; Hansen, E.; Wang, S.; Lei, Z.; Liu, J.; Cao, R.; Zhang, G.; Jiao, S. Deciphering pitting behavior of lithium metal anodes in lithium sulfur batteries. *Journal of Energy Chemistry* **2020**, *49*, 257−261.

(25) Venturi, V.; Viswanathan, V. Thermodynamic Analysis of Initial Steps for Void Formation at Lithium/Solid Electrolyte Interphase Interfaces. *ACS Energy Letters* **2022**, *7* (6), 1953−1959.

(26) Sun, H.-H.; Dolocan, A.; Weeks, J. A.; Rodriguez, R.; Heller, A.; Mullins, C. B. In situ formation of a multicomponent inorganic-rich SEI layer provides a fast charging and high specific energy Li-metal battery. *Journal of Materials Chemistry A* **2019**, *7* (30), 17782−17789.

(27) Li, Y.; Huang, W.; Li, Y.; Pei, A.; Boyle, D. T.; Cui, Y. Correlating Structure and Function of Battery Interphases at Atomic Resolution Using Cryoelectron Microscopy. *Joule* **2018**, *2* (10), 2167−2177.

(28) Park, J.; Jeong, J.; Lee, Y.; Oh, M.; Ryou, M.-H.; Lee, Y. M. Micro-Patterned Lithium Metal Anodes with Suppressed Dendrite Formation for Post Lithium-Ion Batteries. *Adv. Mater. Interfaces* **2016**, *3* (11). DOI: 10.1002/admi.201600140.

(29) Zheng, J.; Yan, P.; Mei, D.; Engelhard, M. H.; Cartmell, S. S.; Polzin, B. J.; Wang, C.; Zhang, J. G.; Xu, W. Highly Stable Operation of Lithium Metal Batteries Enabled by the Formation of a Transient High-Concentration Electrolyte Layer. *Adv. Energy Mater.* **2016**, *6* (8). DOI: 10.1002/aenm.201502151.

(30) Liang, Z.; Nie, Z.; An, A.; Gong, J.; Wang, X. A particle shape extraction and evaluation method using a deep convolutional neural network and digital image processing. *Powder Technol.* **2019**, *353*, 156−170.

(31) Kervrann, C.; Sanchez Sorzano, C. O.; Acton, S. T.; Olivo-Marin, J.-C.; Unser, M. A Guided Tour of Selected Image Processing and Analysis Methods for Fluorescence and Electron Microscopy. *IEEE Journal of Selected Topics in Signal Processing* **2016**, *10* (1), 6−30.

(32) Xu, K. Electrolytes and Interphases in Li-Ion Batteries and Beyond. *Chem. Rev.* **2014**, *114* (23), 11503−11618.

(33) Thirumalraj, B.; Hagos, T. T.; Huang, C. J.; Teshager, M. A.; Cheng, J. H.; Su, W. N.; Hwang, B. J. Nucleation and Growth Mechanism of Lithium Metal Electroplating. *J. Am. Chem. Soc.* **2019**, *141* (46), 18612−18623.

(34) Bard, A. J.; Faulkner, L. R.; White, H. S. *Electrochemical Methods: Fundamentals and Applications*; John Wiley & Sons, 2022.

(35) Tang, L.; Han, B.; Persson, K.; Friesen, C.; He, T.; Sieradzki, K.; Ceder, G. Electrochemical Stability of Nanometer-Scale Pt Particles in Acidic Environments. *J. Am. Chem. Soc.* **2010**, *132* (2), 596−600.

(36) Chen, Q.; Wiedenroth, H. S.; German, S. R.; White, H. S. Electrochemical Nucleation of Stable N2 Nanobubbles at Pt Nanoelectrodes. *J. Am. Chem. Soc.* **2015**, *137* (37), 12064−12069.

(37) Edwards, M. A.; White, H. S.; Ren, H. Voltammetric Determination of the Stochastic Formation Rate and Geometry of

Individual H(2,) N(2), and O(2) Bubble Nuclei. *ACS Nano* **2019**, *13* (6), 6330−6340.

(38) Toschev, S.; Markov, I. An experimental study of non steady state nucleation. *Berichte der Bunsengesellschaft für physikalische Chemie* **1969**, *73* (2), 184−188.

(39) Budevski, E. B.; Staikov, G. T.; Lorenz, W. J. *Electrochemical Phase Formation and Growth: An Introduction to the Initial Stages of Metal Deposition*; John Wiley & Sons, 2008.

(40) Ennos, A. E.; Virdee, M. S. Precision measurement of surface form by laser profilometry. *Wear* **1986**, *109* (1), 275−286.

(41) Wang, B.; Xu, K.; Xu, D.; Cai, X.; Qiao, Y.; Sheng, L. Anisotropic corrosion behavior of hot-rolled Mg-8 wt.%Li alloy. *Journal of Materials Science & Technology* **2020**, *53*, 102−111.

(42) Yang, Y.; Zhou, W.; Yin, S.; Wang, S. Y.; Yu, Q.; Olszta, M. J.; Zhang, Y. Q.; Zeltmann, S. E.; Li, M.; Jin, M.; et al. One dimensional wormhole corrosion in metals. *Nat. Commun.* **2023**, *14* (1), 988.

(43) Mohammadi, A.; Monconduit, L.; Stievano, L.; Younesi, R. Measuring the Nucleation Overpotential in Lithium Metal Batteries: Never Forget the Counter Electrode! *J. Electrochem. Soc.* **2022**, *169* (7), 070509.

(44) Zheng, J.; Archer, L. A. Crystallographically Textured Electrodes for Rechargeable Batteries: Symmetry, Fabrication, and Characterization. *Chem. Rev.* **2022**, *122* (18), 14440−14470.

(45) Gümpel, P.; Hörtnagl, A. Influence of the surface condition on corrosion behavior of stainless steel. *Materials and Corrosion* **2016**, *67* (6), 607−620.

(46) Schwenk, W. Theory of stainless steel pitting. *Corrosion* **1964**, *20* (4), 129t−137t.

(47) Sahu, S.; Frankel, G. S. Phase Field Modeling of Crystallographic Corrosion Pits. *J. Electrochem. Soc.* **2022**, *169* (2), 020557.

https://doi.org/10.1021/acsami.4c01530